Journal of
Materials Chemistry A

Materials for energy and sustainability

## Accepted Manuscript

This article can be cited before page numbers have been issued, to do this please use: M. R. S. Pavel, A. Santhiran, S. Dalberg, A. J. Rossini and J. Vela, *J. Mater. Chem. A*, 2025, DOI: 10.1039/D5TA07992F.




ROYAL SOCIETY OF CHEMISTRY

rsc.li/materials-a

View Article Online
DOI: 10.1039/D5TA07992F

ARTICLE

# Alkali Triel Chalcogenide Nanocrystals: A Molecular Reactivity Approach to Ternary Phase Selectivity

Md Riad Sarkar Pavel,[a] Anuluxan Santhiran,[a,b] Seth Dalberg,[a] Aaron J. Rossini,[a,b] Javier Vela*[a,b]

Received 00th January 20xx,
Accepted 00th January 20xx

DOI: 10.1039/x0xx00000x

Alkali-metal based materials are promising building blocks for energy conversion and storage technologies. Here, we use a molecular reactivity-based, solution-phase approach to selectively synthesize multiple phases and specific polymorphs of lithium- and sodium-containing triel chalcogenide nanocrystals ($LiTrCh_2$, $NaTrCh_2$, $NaTr_3Ch_5$; Tr = Ga, In; Ch = S, Se, Te). Analogous to the case of binary II-VI and III-V tetrahedral semiconductors, where the two commonly isolated zinc blende and wurtzite polymorphs are separated by only 1-50 meV/f.u., we find that $LiTrCh_2$ nanocrystals easily adopt tetragonal (chalcopyrite) and orthorhombic polymorphs separated by only 2.7-6.2 meV/f.u.. Because of this small energy difference, soft colloidal synthesis succeeds in accessing either one of these polymorphs depending on the specific dichalcogenide precursor used. Highly reactive diethyl diselenide favors the thermodynamic, more stable tetragonal $I\bar{4}2d$ phase, whereas mildly reactive diphenyl diselenide favors the kinetic, metastable orthorhomic *Pna*21 phase. Density functional theory calculations confirm the relative energy among multiple $LiTrCh_2$ polymorphs, and also model the observed powder X-ray diffraction pattern of a new C2 $NaIn_3Te_5$ phase. $^{7}$Li, $^{69}$Ga, and $^{77}$Se solid-state NMR spectra are consistent with phase pure, ternary $LiGaSe_2$ nanocrystals. A majority of the nanocrystal compositions are visible light emitters. This work opens the door to new Li/Na-based ternary triel chalcogenide nanostructures for energy storage and conversion applications.

## Introduction

From their discovery in 1807[1] to the next generation of batteries[2,3,4] and solar cells,[5] alkali metals are indispensable elements at the forefront of research and development in new energy conversion and storage materials and devices. Alkali ion batteries provide on demand power to small portable electronics and electric vehicles.[6] High energy density, lightweight Li batteries are most widespread.[7,8] Similarly, Na and K batteries continue to gain momentum due to their wide elemental geodistribution, low potential, fast ion diffusion, and low toxicity compared to Pb acid batteries.[9,10] Alkali metal chalcogenides have shown promise beyond battery anodes,[11] for example as Earth-abundant, environmentally benign, and biocompatible materials for photovoltaic devices.[12] By mitigating adverse interfacial recombination pathways, alkali ions help to effectively reduce photovoltaic losses and increase the open-circuit current and fill factor of perovskite[13] and copper indium gallium diselenide (CIGS) solar cells.[14]

In this context, alkali triel chalcogenides (Alk-$III_x$-$VI_y$, Alk = Li, Na, K, III = Ga, In; VI = S, Se, Te, etc.) belong to an interesting family of ternary semiconductors with rich structural chemistry and useful optoelectronic properties. While related I-III-$VI_2$ materials (i.e. $CuInSe_2$, $AgGaSe_2$, etc.) adopt the chalcopyrite structure ($I\bar{4}2d$), lithium triel chalcogenides (Li-III-$VI_2$) crystallize in a wide range of space groups. Depending on their composition and specific crystallization conditions, they can adopt orthorhombic (*Pna*21/*P*21*nb*), cubic ($Fm\bar{3}m$), and trigonal ($R\bar{3}mH$) phases.[12] (Figure 1). In turn, sodium triel chalcogenides (Na-$III_x$-$VI_y$, x = 1, 3, y = 2, 5) adopt mainly trigonal ($R\bar{3}mH$/*P*32) or monoclinic (*C*2) phases, with some tetragonal and orthorhombic variations. From a colloidal synthesis perspective, this polymorphism offers an opportunity to observe, study, and isolate metastable or kinetic phases with unprecedented chemical and physical properties.[15,16] From the perspective of applications, replacement of Cu or Ag with Li widens the semiconducting band gap, increasing the threshold for laser induced damage and overall photostability. Thus, in addition to batteries or solar cells,[17] alkali triel chalcogenides may be useful in near- and mid-IR nonlinear optics,[18,19,20] water splitting[21] and $CO_2$ photocatalysis,[22] and also in neutron detectors,[23] and even phase change memory materials.[24] Already, experimental examples underscoring the potential of this new family of nanostructured materials include the use of $LiInS_2$ or $LiInSe_2$ nanosheets in batteries,[25,26] $NaGaS_2$ in radiation detectors,[27] and $KGaS_2$ nanocrystals in the conversion of $CO_2$ to CO.[28]

Common approaches to achieve synthetic control during nanocrystal preparations include optimization of reaction conditions (reaction time, temperature), as well as utilization of different ligands and solvents.[29,30] A powerful tool in nanocrystal synthesis is leveraging predictable trends in the reactivities of molecular precursors based on their molecular structure, in order to control the kinetics of nanocrystal nucleation and growth.[31,32] Disubstituted (diorganyl) dichalcogenides (RChChR; R = ethyl, methyl, phenyl, etc.; Ch = S, Se, etc.) are prime examples of this approach as their reactivities strongly depend on the identity of the organic substituent (R).[33,34,35,36] In this way, different dichalcogenide precursors can enable the preparation of metastable phases depending on their C-Ch bond dissociation energies.[31]

[a] Department of Chemistry, Iowa State University, Ames, Iowa 50011 USA.
[b] Ames National Laboratory, Ames, Iowa 50011 USA.

View Article Online
DOI: 10.1039/D5TA07992F

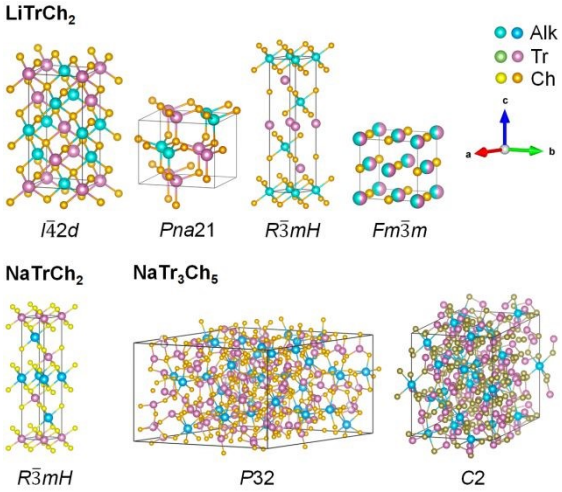


**Fig. 1.** Common crystal structures of ternary lithium- and sodium-based triel chalcogenide semiconductors.

At present, high temperature reactions between the elements result in bulk (polycrystalline) or single crystals of alkali triel chalcogenides. A few solvothermal and molten-salt syntheses,[37] as well as high-temperature reactions in flux also produce alkali triel chalcogenides with large particle size, although binary impurities are sometimes present.[38,39,40] A few colloidal synthesis of (Alk)-Tr-$Ch_2$ nanocrystals appeared recently.[41,42,43] Interestingly, only pressure-induced Alk-III-$VI_2$ phase transformations are reported.[44] Here, we describe a molecular reactivity approach to phase selective synthesis of lithium- and sodium-based alkali triel chalcogenide (Ch = S, Se, and Te) nanocrystals using readily available alkali metal, triel, and disubstituted dichalcogenide RChChR precursors.

## Results and discussion

**Colloidal alkali triel chalcogenide nanocrystals.** Reaction of Li(acac) and $Ga(acac)_3$ or $In(acac)_3$ with disubstituted dichalcogenides (RChChR) in oleylamine ($oleylNH_2$) and 1-octadecene (ODE) at 270–330 °C produces $LiTrCh_2$ nanocrystals (Scheme 1). Because of its mild reactivity and solubility, Li(acac) is more reliable and versatile than other Li precursors such as nitrates, halides, or carbonates.[45] Harsher precursors such as LiH, $Li(NPr_2)$, PhLi, or n-BuLi react too fast under these conditions, resulting in lower order, binary triel chalcogenides ($Tr_2Ch_3$) rather than the desired ternary nanocrystals.

**Scheme 1.** Solution-phase synthesis of colloidal alkali triel chalcogenide nanocrystals.

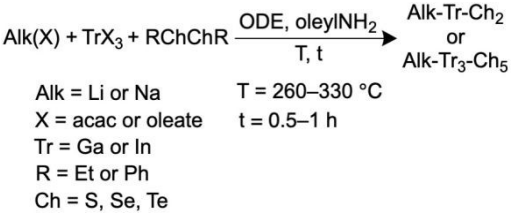


The experimental powder X-ray diffraction (XRD) patterns of the nanocrystals match the reported Pna*21* and I$\bar{4}$2*d* ($LiGaSe_2$ and $LiInSe_2$) or *P*21*nb* ($LiInS_2$) phases of these materials (Figure 2). The specific polymorph observed is highly dependent on the structure and reactivity of the specific disubstituted dichalcogenide precursor used—see further phase selectivity and computations sections below. The single crystalline domain (Scherrer) sizes calculated from powder XRD peaks widths for $LiTrCh_2$ nanocrystals range from 7–20 nm, respectively (Table 1).

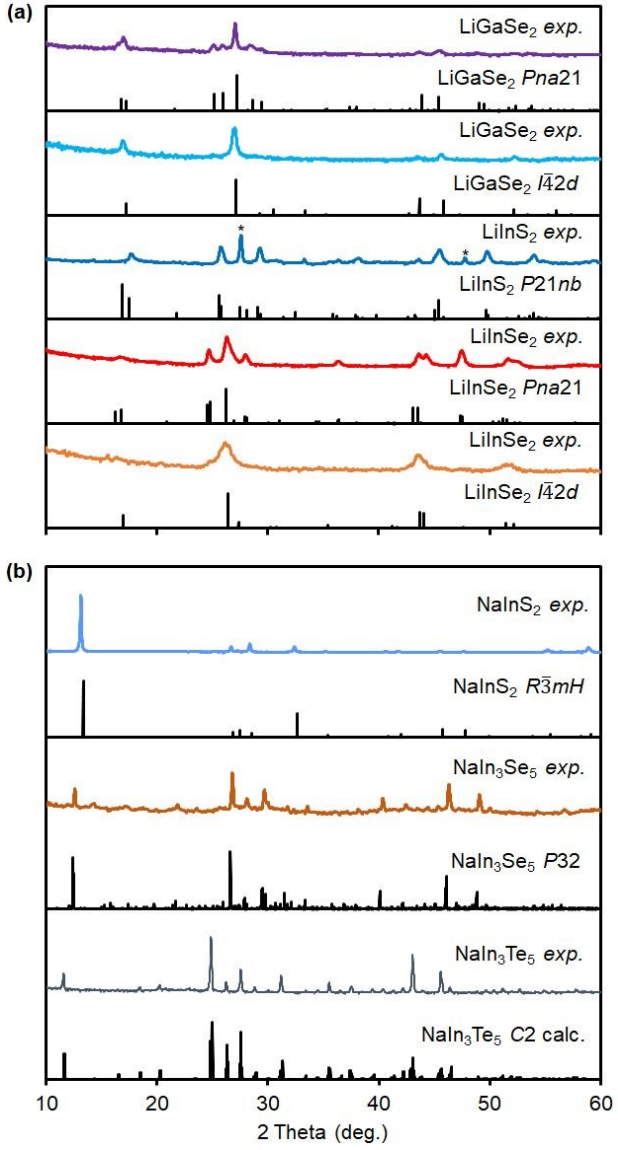


**Fig. 2.** Powder XRD of (a) Pna*21* $LiGaSe_2$ (ICSD-53093), I$\bar{4}$2*d* $LiGaSe_2$ (ICSD-89176), *P*21*nb* $LiInS_2$ (ICSD-53093), Pna*21* $LiInSe_2$ (ICSD-60838), and I$\bar{4}$2*d* $LiInSe_2$ (ICSD-56532) nanocrystals; (b) R$\bar{3}$*mH* $NaInS_2$ (ICSD-25557), *P*32 $NaIn_3Se_5$ (ICSD-243563), and *C*2 $NaIn_3Te_5$ nanocrystals (calculated using VASP, see Methods). *$In_2S_3$ impurity (ICSD-23844).

Using a similar approach, the reaction of Na(oleate) with $In(acac)_3$ and PhChChPh (Ch = S, Se, Te) enables the preparation of nanocrystalline sodium triel chalcogenides. Powder XRD patterns match those reported for R$\bar{3}$*mH* $NaInS_2$, *P*32 $NaIn_3Se_5$ and—for the first time—a previously unreported *C*2 $NaIn_3Te_5$ phase (Figure 2). This new ternary compound has a relatively large monoclinic unit cell comprised of octahedral [$NaTe_6$], tetrahedral [$InTe_4$], and four coordinate [$Na_2SeIn_2$] sites—see Supplementary Information (SI). Rietveld refinement of the experimental powder XRD pattern matches well with the calculated *C*2 XRD (see calculations below). The higher reactivity of Na(oleate) compared to Li(acac) results in generally larger 510–960 nm particles for Na- vs. Li-based materials (Table 1).

**Phase selectivity and morphology.** The colloidal $LiTrCh_2$ nanocrystals made by our method typically adopt the tetragonal $I\bar{4}2d$ chalcopyrite and/or orthorhombic *Pna*21 ($LiTrSe_2$) and the *P*21*nb* ($LiInS_2$) structures (Table 1). This agrees with our calculations showing that these two phases have very similar energies. In the case of $LiGaSe_2$ and $LiInSe_2$, the chalcopyrite ($I\bar{4}2d$) polymorph is the most thermodynamically stable, but only by about 2.7–6.2 meV compared to the orthorhombic (*Pna*21) phase—see computations below. For comparison, the two most isolated, zinc-blende and wurtzite polymorphs of binary tetrahedral semiconductors (II-VI, III-V) are only 1–50 meV/formula unit (f.u.) apart.[46,47]

To effectively deliver chalcogen to the reaction medium, both of the C-Ch and Ch-Ch bonds in the dichalcogenide precursor must break. *Aromatic disubstituted dichalcogenides* such as PhChChPh have strong C(Aryl)-Ch bonds (64.4–69.8 kcal/mol) and weak Ch-Ch bonds (43.6–45.7 kcal/mol, as judged by their bond dissociation energies).[31] As a result, PhChChPh precursors release [Ch] very slowly but quickly release [PhCh·]; these can act as surface passivating agents that stabilize small reactive clusters and seeds, slowing nanocrystal growth. Therefore, the use of aryl substituted dichalcogenides such as PhSeSePh succeeds in the preparation of metastable, kinetic orthorhombic (*Pna*21) polymorphs of $LiGaSe_2$ and $LiInSe_2$ (Scheme 2 and Table 1). These observations agree with the isolation of metastable polymorphs of $CuInSe_2$—and, very recently, $CsGaCh_2$—from reactions using PhSeH[35] and PhSeSePh,[43] respectively, both of which bear strong, hard to break C-Se bonds.

In contrast, *aliphatic substituted dichalcogenides* have much weaker the C-Ch bonds in (by about 11–12 kcal/mol),[31] compared to those bearing aromatic substituents. Consequently, both C-Ch and Ch-Ch bonds in EtChChEt precursors break more easily, releasing [Ch] relatively fast and accelerating the rates of nucleation and growth. Thus, the use of the much more reactive EtSeSeEt precursor results in the isolation of the more stable, thermodynamic chalcopyrite ($I\bar{4}2d$) polymorphs of $LiGaSe_2$ and $LiInSe_2$ (Scheme 2). Using PhSSPh also results in the formation of the orthorhombic (*P*21*nb*) phase of $LiInS_2$, the only experimentally reported polymorph for this material, albeit with a small binary $In_2S_3$ impurity (Table 1). To further increase the phase purity of $LiInS_2$, future work will explore the use of precursors with weaker C-S bonds compared to that of PhSSPh. Alternatively, more reactive Li precursors could also decrease the amount of $In_2S_3$ byproduct by virtue of releasing Li much faster into the reaction mixture.

**Scheme 2.** Phase-selective synthesis of colloidal $LiTrCh_2$ nanocrystals.

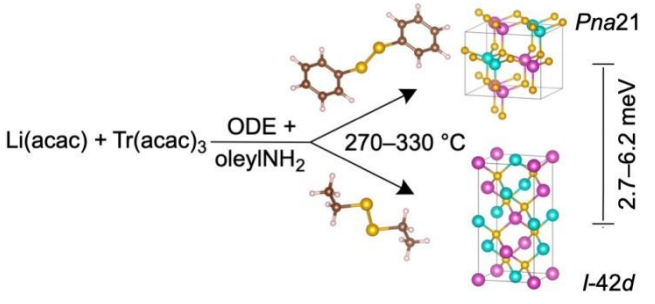


Bright-field transmission electron microscopy (TEM) shows that the morphology of $LiTrCh_2$ nanocrystals mainly depends on their composition, more so than on the specific polymorph present. For example, both *Pna*21 and $I\bar{4}2d$ $LiGaSe_2$ nanocrystals are spheroidal, even though high resolution (HR) TEM and fast Fourier transform (FFT) of selected area electron diffraction (SAED) patterns confirm the presence of different sets of planes for the *Pna*21—(110), (221)—and $I\bar{4}2d$ phases—(112), (101), (204)—Figure 3a and 3b, respectively. *P*21*nb* $LiInS_2$ nanocrystals are also spheroidal (see SI). In contrast, both *Pna*21 and $I\bar{4}2d$ $LiInSe_2$ nanocrystals adopt a triangular plate morphology, even though HR TEM and FFT SAED analyses confirm the presence of different sets of planes for the *Pna*21—(002), (210), (113), and (231)—and $I\bar{4}2d$ phases—(112), (103), and (204)—Figure 3c and 3d, respectively. Energy dispersive X-ray spectroscopy (EDS) under the scanning electron microscopy (SEM) is consistent with the nanocrystals' compositions; for example, $(Li)Ga_{1.0}Se_{2.4}$ and $(Li)In_{1.0}Se_{1.9}$ for the *Pna*21 phases of $LiGaSe_2$ and $LiInSe_2$, respectively (the light Li atoms are undetected).

Interestingly, the fact that $LiGaSe_2$ and $LiInS_2$ nanocrystals are spheroidal while $LiInSe_2$ nanocrystals containing the heavier Se chalcogen are highly anisotropic (plate-like) has some precedence in the literature. For example, $NaSbSe_2$ nanocrystals are quasispheroidal while $NaBiSe_2$ nanocrystals are anisotropic (elongated, rods).[48,49] Particle shapes with lower aspect ratios are normally preferred thermodynamically.[49] In our case, the less reactive, lighter Ga and S precursors required significantly higher reaction temperatures (300-330 °C, Table 1) compared to the more reactive, Se precursors (270 °C), which likely explains why the former trended toward the lower aspect ratio, spheroidal shapes.

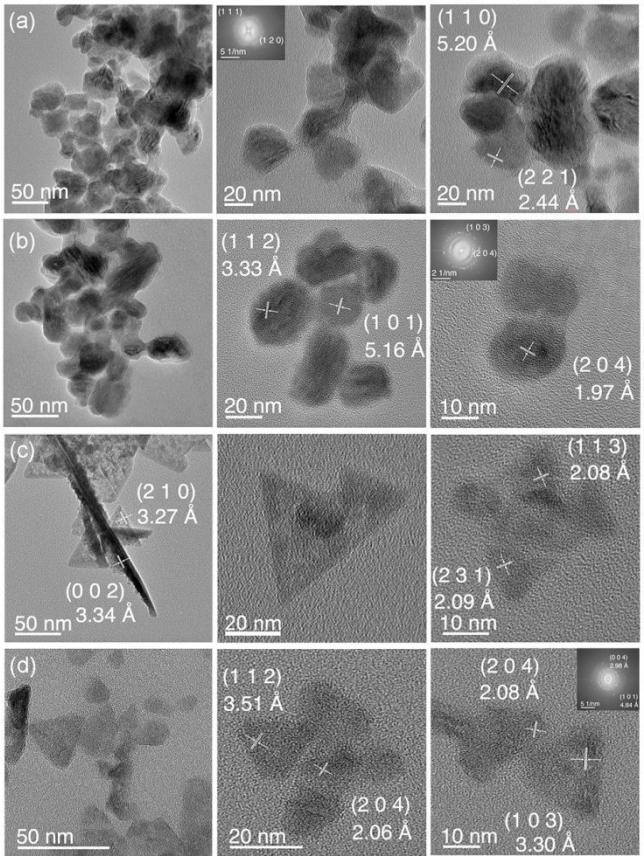


**Fig. 3.** Representative TEM images of (a) *Pna*21 $LiGaSe_2$ (TEM particle size: 10±4.2 nm), (b) $I\bar{4}2d$ $LiGaSe_2$ (22±5.6 nm), (c) *Pna*21 $LiInSe_2$ (13±6.7 nm), and (d) $I\bar{4}2d$ $LiInSe_2$ (19±5.5 nm) nanocrystals.

View Article Online
DOI: 10.1039/D5TA07992F




**Table 1.** Synthesis of ternary alkali triel chalcogenide nanocrystals.

| Precursors (mmol) | | | Conditions[a] | | Products | |
|---|---|---|---|---|---|---|
| Alkali metal | Triel | Chalcogen | T (°C) | t (min) | Phase | Scherrer, TEM/SEM (nm) |
| Li(acac) (0.1) | $Ga(acac)_3$ (0.1) | PhSeSePh (0.2) | 330 | 60 | *Pna*21 $LiGaSe_2$ | 15±4.9, 11±4.2 |
| Li(acac) (0.1) | $Ga(acac)_3$ (0.1) | EtSeSeEt (0.6) | 300 | 60 | $I\bar{4}2d$ $LiGaSe_2$ | 20±5.5, 22±5.6 |
| Li(acac) (0.15) | $In(acac)_3$ (0.2) | PhSSPh (0.6) | 330 | 60 | *P*21*nb* $LiInS_2$ + $In_2S_3$[b] | 8.1±1.3 |
| Li(acac) (0.1) | $In(acac)_3$ (0.1) | PhSeSePh (0.2) | 270 | 60 | *Pna*21 + $I\bar{4}2d$ (4:1)[c] $LiInSe_2$ | 18±8.3, 13±6.7 |
| Li(acac) (0.1) | $In(acac)_3$ (0.1) | EtSeSeEt (0.4) | 270 | 60 | $I\bar{4}2d$ $LiInSe_2$ | 7.4±1.6, 19±5.5 |
| Na(oleate) (0.1) | $In(acac)_3$ (0.1) | PhSSPh (0.2) | 280 | 30 | $R\bar{3}mH$ $NaInS_2$ | 507±83 |
| Na(oleate) (0.1) | $In(acac)_3$ (0.1) | PhSeSePh (0.1) | 290 | 60 | *P*32 $NaIn_3Se_5$ | 957±182 |
| Na(oleate) (0.1) | $In(acac)_3$ (0.1) | PhTeTePh (0.05) | 260 | 30 | *C*2 $NaIn_3Te_5$ | 946 × 256[d] |

[a]4 mL ODE + 4 mL oleylNH$_2$. [b]Minor impurity. [c]Estimated from Match. [d]Total span × arm width of hexapods.

SEM images reveal that $NaInS_2$, $NaIn_3Se_5$, and $NaIn_3Te_5$ nanocrystals adopt different morphologies (Figure 4 and SI). Very much like the Li-ternary nanocrystals, Na-containing ternary nanocrystals undergo shape evolution from lower to higher anisotropy on going down the chalcogen group from S to Se to Te. Specifically, $NaInS_2$ crystals are spheroidal, $NaIn_3Se_5$ crystals exhibit some anisotropy and are cuboidal, and $NaIn_3Te_5$ crystals are very anisotropic and adopt a hexapod-like shape. Thus, the idea that composition plays a key role in determining the shape of Li- and Na-containing ternary chalcogenide nanocrystals is strongly supported by the available data. Lighter atom-containing nanocrystals often adopt more thermodynamically favorable, isotropic shapes, while those containing heavier atoms tend to be much more anisotropic. Recent reports on $AInSe_2$ (A = K, Rb, Cs) nanocrystals also showed a variety of morphologies depending on the different cations that were present and the chalcogen precursors used.[41] Selected EDS area scans under the SEM show average compositions of $Na_{1.2}In_{1.0}S_{2.0}$, $Na_{1.4}In_{3.0}Se_{5.1}$, and $Na_{4.5}In_{2.5}Te_{5.0}$ (see SI). An excess of Na and Ch atoms in the latter may be attributable to some remaining unreacted sodium precursor or amorphous impurity, as it is absent in the powder XRD.

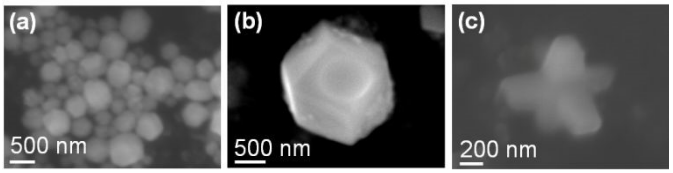


**Fig. 4.** Representative SEM images of (a) $NaInS_2$, (b) $NaIn_3Se_5$, and (d) $NaIn_3Te_5$ nanocrystals.

**Stability and phase transformations.** The phase selective synthesis and structural transformations of alkali metal-based ternary chalcogenides continue to be the subject of intense research activity. For example, $CsGaCh_2$ (Ch = S, Se) adopts a $TlGaSe_2$-type (*mC*64) layered (2D) structure at low temperature and a $KFeS_2$-type (*mC*16) structure containing one dimensional (1D) chains at high-temperature. Density functional theory (DFT) shows these two polymorphs are only 0.01 eV/atom apart.[42] In the bulk, *mC*64 $CsGaCh_2$ reversibly phase transitions to the *mC*16 polymorph at ~600 °C. At the nanoscale, *mC*64 $CsGaCh_2$ irreversibly converts to the thermodynamic *mC*16 polymorph at 320 °C in solution[43] and at 1000 °C in the solid state.[42]

In this work, we find that $LiTrCh_2$ nanocrystals possess significant air and thermal stability, as evidenced by continued monitoring of their powder XRD over time and by thermal analyses—see SI. Notably, $LiInSe_2$ nanocrystals remain phase pure even after 5 months under ambient conditions of temperature and air, while $LiGaSe_2$ nanocrystals only start showing signs of partial decomposition to lower order, binary impurities after 2 months. Both are remarkably thermally stable in $N_2$, losing ≤3% mass to 1000 °C.

**SSNMR Spectroscopy.** Solid-state NMR (SSNMR) spectroscopy experiments were performed on ternary $LiGaSe_2$ and $LiInSe_2$ samples to identify their chemical environments. $^7$Li is a spin 3/2 nucleus with 92.4% natural abundance.[50] $^7$Li has a chemical shift of 1 ppm and 3 ppm for the $LiGaSe_2$ and $LiInSe_2$, respectively, differing by 2 ppm (Figure 5a). $^{69}$Ga is a spin 3/2 nucleus with 60.1% natural abundance.[50] Quadrupolar nuclei like $^{69}$Ga often have sizable first and second-order quadrupolar interactions, which lead to broader central transition SSNMR spectra.[51,52] The $^{69}$Ga SSNMR spectrum was acquired with a wideband uniform rate smooth truncation QCPMG (WCPMG) pulse sequence.[53,54] The WCPMG echoes were coadded using a C code to make the coadded echo SSNMR spectrum (Figure 5b). The electric field gradients (EFG) tensor parameters were measured by fitting the coadded SSNMR spectrum, summarized in Table 2. $^{77}$Se is a spin ½ nucleus with 7% natural abundance.[50] Most $^{77}$Se compounds have large spin-lattice relaxation rates ($T_1$), which results in a longer experimental time.[55,56] $^{77}$Se NMR spectrum of $LiGaSe_2$ was acquired using a Carr-Purcell Meiboom-Gill (CPMG) pulse sequence. The $^{77}$Se SSNMR spectrum shows a single peak that has an isotropic chemical shift ($d_{iso}$) of 794 ppm with a span (W) of ~475 ppm.

**Table 2.** EFG/Chemical shift tensors of $LiGaSe_2$ nanocrystals.

| Material | Nuclei | $\delta_{iso}$ (ppm) | $\Omega$ (ppm) | $\kappa$ | $\eta_Q$ | $C_Q$ (MHz) |
|---|---|---|---|---|---|---|
| $LiGaSe_2$ | $^{69}$Ga | 233 | - | - | 1.0 | 4.9 |
| | $^{77}$Se | 794 | 473 | 0.2 | - | - |

View Article Online
DOI: 10.1039/D5TA07992F




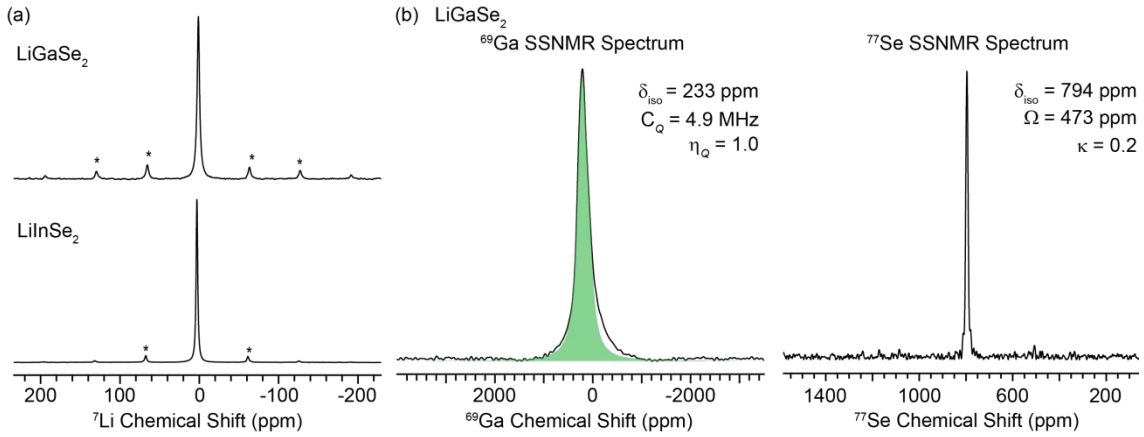


**Fig. 5.** (a) Comparison of $^{7}$Li spin-echo SSNMR spectra of $LiGaSe_2$ and $LiInSe_2$ nanocrystals. (b) $^{69}$Ga WCPMG SSNMR and $^{77}$Se CPMG SSNMR spectra (left) of $LiGaSe_2$ nanocrystals. Spinning side bands are marked with "*".

**Optical properties.** The band gaps of 1.8–3.4 eV in the synthesized $LiTrCh_2$ nanocrystals closely match the values reported in the literature[57,58] (Table 3). It is noteworthy that, despite their distinct structures, the tetragonal ($I\bar{4}2d$) and orthorhombic (*Pna*21) forms of $LiTrCh_2$ have similar band gaps, which is consistent with previous reports on single crystals.[59] All $LiTrCh_2$ nanocrystals display UV or Vis photoluminescence, with maxima ($PL_{max}$) between 380 nm and 620 nm and quantum yields (QY) ranging from 1.2–4.6% (Figure 6).

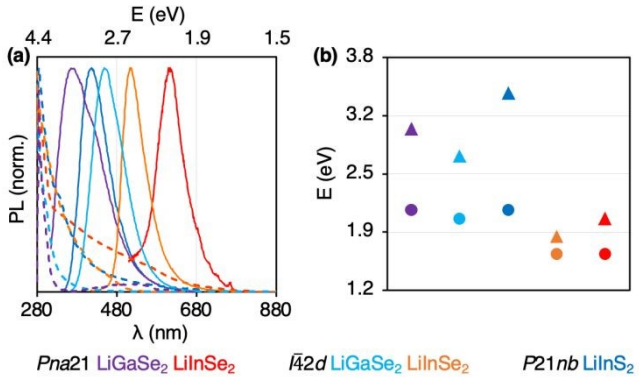


**Fig. 6.** (a) Optical absorption (dashed lines) and photoluminescence (solid) of $LiTrCh_2$ nanocrystals. (b) Experimental (▲) vs. calculated (●) band gaps.

Multiple literature reports indicate that the band gap and PLmax of $LiTrCh_2$ semiconductors are strongly dependent on defects.[60] For example, $LiInSe_2$ has an intrinsic bandgap of around 2.8 eV,[61] but this narrows with increasing defect density.[62,63] Density functional theory (DFT) calculations suggest that $In_{Li}$ and $Li_{In}$ antisites are the main defects responsible for this behavior.[63] Defect types in yellow single crystals of $Li_{1.01}In_1Se_2$ are $V_{Se}^{+}$ and $Li_{In}^{2-}$, while those in red crystals are $In_{Li}^{2+}$ and $V_{Li-}$.[23] In this study, we observe that the *Pna*21 and $I\bar{4}2d$ *phases of* $LiInSe_2$ have band gaps of 1.8 and 2.0 eV. Thus, we assume that both synthesized nanocrystals possess defects to some degree, with a higher density in the *Pna*21 $LiInSe_2$ nanocrystals. Further work will address ways to decrease the number of defects as a way to further increase the PL QYs of these materials.

**Table 3.** Optical properties of alkali triel chalcogenides.

| Nanocrystal phase | Band gap (eV) | | | |
|---|---|---|---|---|
| | Exp. | | Theo. | |
| | (Abs.) | Lit. | (DFT) | Lit. |
| *Pna*21 $LiGaSe_2$ | 3.0 | 2.1–3.7 | 2.0–2.1 | 2.4–3.4 |
| $I\bar{4}2d$ $LiGaSe_2$ | 2.7 | 1.7–2.0 | 2.0 | 2.8 |
| *P*21*nb* $LiInS_2$ | 3.4 | 3.6 | 2.1 | 1.3–3.3 |
| *Pna*21 $LiInSe_2$ | 1.8 | 1.6–2.8 | 1.5–1.6 | 2.6 |
| $I\bar{4}2d$ $LiInSe_2$ | 2.0 | 2.9 | 1.5–1.6 | - |
| $R\bar{3}mH$ $NaInS_2$ | 2.5 | 2.4 | - | 0.7–3.3 |
| *P*32 $NaIn_3Se_5$ | 2.1 | 2.2 | - | - |
| *C*2 $NaIn_3Te_5$ | 1.7 | - | 0.6 | - |

Sodium-based ternary nanocrystals, on the other hand, have band gaps of 1.7–2.5 eV (see SI). Importantly, $NaInS_2$ and $NaIn_3Se_5$ nanocrystals show visible-range PL, while $NaIn_3Te_5$ lacks PL in either Vis or NIR regions. Previously, $NaInS_2$ nanoplates showed a band gap of 2.35 eV[64] and $NaIn_3Se_5$ single crystals 2.17 eV.[40]

**Correlating theory and experiment.** Seeking to obtain deeper physical insight into our results, we used the Vienna Ab-initio Simulation Package (VASP)[65] and the Tight Binding Linear Muffin-tin Orbital Atomic Sphere Approximation (TB-LMTO-ASA)[66] to estimate the relative energies, bonding, and optical properties of all phases for each $LiTrCh_2$ composition. We used coloring patterns[16,67,68] for phases with mixed-cation sites (below).

VASP and LMTO calculations show direct band gaps in the range of 1.5–2.1 eV for these $LiTrCh_2$ nanocrystals and a small theoretical band gap of 0.6 eV for the hypothetical *C*2 $NaIn_3Te_5$ (Table 3). These band gaps are underestimated by 20–54% compared to the

View Article Online
DOI: 10.1039/D5TA07992F
ARTICLE Journal Name



experimentally observed values (Figure 6). Such underestimation is common in semiconductor chalcogenides due to the ignorance of excited states in DFT calculations.[69] Density of states (DOS) shows that Ch-p orbital dominates the valence bands with some contributions from Tr-s and Tr-p orbitals in all the phases (see SI). Previous DFT calculations on $LiTrCh_2$ and $NaTrCh_2$ also indicated a substantive contribution of the covalent component from Ch-p and Tr-p orbitals in the chemical bonding of these materials.[70,71,72]

A comparison of relative energies among the PBE-relaxed crystal structures for each composition yields useful insights into the outcome of our nanocrystal preparations. $LiGaSe_2$ has two reported phases, $I\bar{4}2d$ and *Pna*21, which are only 6.2 meV apart, with $I\bar{4}2d$ being the lowest energy polymorph.[73] As noted above, this explains our ability to selectively prepare either phase using molecular precursors with different reactivity. More specifically, the more highly reactive EtSeSeEt leads to quick formation of nanocrystals adopting the thermodynamic $I\bar{4}2d$ phase, while the more mildly reactive PhSeSePh enables the isolation of nanocrystals adopting the kinetic (metastable) *Pna*21 phase (Scheme 2). In contrast, $LiInS_2$ has only one crystallographically reported, *P21nb*, as observed experimentally.

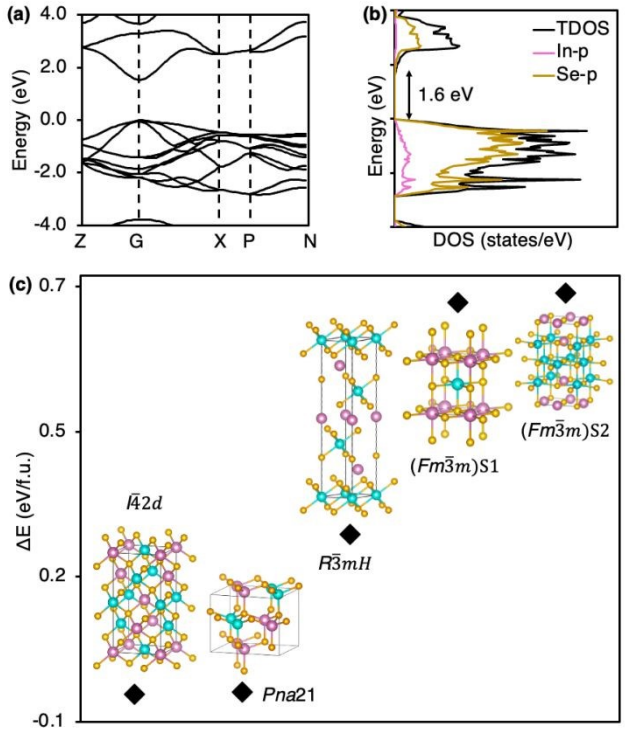


**Fig. 7.** Calculated (a) band structure and (b) density of states for $I\bar{4}2d$ $LiInSe_2$, along with (c) relative energies for its different polymorphs.

The inorganic crystal structure database (ICSD) contains four reported polymorphs for $LiInSe_2$, including a disordered cubic $Fm\bar{3}m$ phase with mixed cation (Li/In) sites. In this case, we first created two different supercells using different coloring patterns while keeping the stoichiometry intact,[67] which we labeled ($Fm\bar{3}m$)S1 and ($Fm\bar{3}m$)S2 (Figure 7). As in the case of the lighter, gallium-containing analogue, $I\bar{4}2d$ $LiInSe_2$ has the lowest energy, followed closely by *Pna*21 $LiInSe_2$—only ca. 2.7 meV higher than the first. Interestingly, the even smaller energy difference compared to the previous gallium case explains why it is even more challenging in the indium case to isolate metastable *Pna*21 $LiInSe_2$ nanocrystals in 100% pure form (Table 1).

The other polymorphs of $LiInSe_2$, including $R\bar{3}mH$—291 meV higher—and the colored supercells ($Fm\bar{3}m$)S1 and ($Fm\bar{3}m$)S2—715-732 meV higher—contain octahedrally coordinated cation sites and shorter bonds. These high-pressure phases, which are metallic in character (see SI) are too high energy to be relevant under the relatively low temperature and ambient pressure, colloidal synthesis conditions used here. Lastly, because the ICSD lacks a reported structure for $NaIn_3Te_5$, we computationally built a unit cell by replacing Ga with In in the reported *R*32*H* crystal structure of $NaGa_3Te_5$. The calculated XRD pattern matches well with the powder XRD pattern obtained experimentally (Figure 2b).

## Conclusions

In summary, we have synthesized eight different polymorphs of Li/Na-based ternary chalcogenide nanocrystals using a reliable colloidal synthesis method. A combination of powder XRD, high resolution (HR) TEM, fast Fourier transform (FFT) of selected area electron diffraction (SAED) patterns, energy dispersive X-ray spectroscopy (EDS) and, in the case of $LiGaSe_2$ nanocrystals, $^{7}Li$, $^{69}Ga$, and $^{77}Se$ solid state (SS) NMR confirm the identity and phase purity of the different crystalline materials. All nanocrystals except $NaIn_3Te_5$ are photoluminescent, with modest PL QYs between 1.2–4.6%.

Critically, we can selectively isolate either of the tetragonal (chalcopyrite) ($I\bar{4}2d$) or orthorhombic (*Pna*21) phases of $LiGaSe_2$ and $LiInSe_2$ nanocrystals using different dichalcogenide (RSeSeR) precursors. Specifically, highly reactive EtSeSeEt yields the most stable, thermodynamic $I\bar{4}2d$ phase while mildly reactive PhSeSePh yields the metastable (kinetic) *Pna*21 phase. Density functional theory (DFT) calculations on both compositions confirm the relative energy order between these polymorphs—separated by only 2.7-6.4 meV/formula units—as well as other, higher energy phases in the case of $LiInSe_2$. Further, DFT predicts a powder XRD pattern of a previously unreported, *C*2 $NaIn_3Te_5$ phase that matches the powder XRD observed experimentally.

View Article Online
DOI: 10.1039/D5TA07992F

ARTICLE





## Experimental

**Materials.** Oleylamine (oleyl$NH_2$, 70%), 1-octadecene (ODE, 90%), diphenyl diselenide (98%), diphenyl ditelluride (98%), and indium(III) acetylacetonate (99.99+% In) were purchased from Sigma-Aldrich; gallium(III) acetylacetonate (99.99%+ Ga), indium(III) acetylacetonate (99.99+% In), lithium acetylacetonate (99.99+% Li), and sodium oleate (99%) from Strem; diphenyl disulfide (99%) from Acros. **Caution:** Oleylamine is very corrosive and should be handled with great care.

**Synthesis of $LiTrCh_2$ nanocrystals.** Lithium acetylacetonate (0.10 mmol, 11 mg for $LiInSe_2$ and $LiGaSe_2$; 0.15 mmol, 16 mg for $LiInS_2$) and gallium or indium acetylacetonate (0.10 mmol, 37 mg for Ga; 0.10–0.20 mmol, 41–82 mg for In) were dissolved stirred in a mixture of oleyl$NH_2$ (2 mL) and ODE (4 mL) in a round bottom (RB) flask at 100 °C for 1 h under dynamic vacuum. After refilling the RB flask with $N_2$, diphenyl disulfide/diselenide (0.20–0.60 mmol, 44–131 mg for S; 0.20 mmol, 62 mg for Se) in oleyl$NH_2$ (2 mL) was swiftly injected. The temperature was raised to 270–330 °C and stirring continued for 30–60 min. The crude solution was treated with an equivalent amount of ethanol and centrifuged at 4500 rpm for 5 min. After discarding the supernatant, the precipitate containing nanocrystalline solids was redispersed in hexanes, treated with an equivalent amount of ethanol and a few drops of methanol, and centrifuged again at 4500 rpm for 5 min.

**$NaTrCh_2$ or $NaTr_3Ch_5$ nanocrystals**. These were synthesized in by a similar procedure with sodium oleate (0.10 mmol, 37 mg), indium acetylacetonate (0.10 mmol, 37 mg), and diphenyl disulfide/diselenide/ditelluride (0.2 mmol, 44 mg for S; 0.10 mmol, 31 mg for Se; 0.05 mmol, 21 mg for Te) dissolved in oleyl$NH_2$ (2 mL). Reaction temperatures for specific compositions appear in Table 1.

**Structural characterization**. Powder X-ray diffraction (XRD) was collected on a Rigaku Ultima IV diffractometer (40 kV, 44 mA) with a zero-background quartz sample holder using Cu K radiation. A K value of 0.9 was used to determine average single crystalline domain sizes using the Scherrer equation. JOEL JSM-IT200 scanning electron microscope was used for area scans and elemental mapping. Samples were put on double-sided carbon tape and examined at a voltage of 10–15 keV. A JEOL 2100 transmission electron microscope was utilized to carry out transmission electron microscopy imaging. Size distributions contain information from at least 100–200 particles. The samples were prepared by drop-casting a dilute nanocrystal solution in hexane on a Cu grid with a 200-mesh carbon coating.

**Optical characterization.** A photodiode-array Agilent 8453 UV/vis spectrophotometer was used to measure the absorption spectra of the nanocrystals in solution. All spectra are reported after subtracting the absorption of the solvent. Diffuse reflectance spectra were recorded using an SL1 Tungsten Halogen lamp (vis–IR), an SL3 Deuterium Lamp (UV), and a BLACK-Comet C-SR-100 spectrometer (200–1080 nm). Band gap values were estimated by extrapolating the linear slope of Tauc plots of $(Ah\nu)^{1/r}$ versus $h\nu$ ($A$ = absorbance, $h\nu$ = incident photon energy in eV, $r$ = 1/2 for direct and $r$ = 2 for indirect semiconductors).[74] A Horiba-Jobin Yvon Nanolog scanning spectrofluorometer with a photomultiplier detector was used to measure steady-state PL spectra. Rhodamine 440 or rhodamine 460 dye was utilized as standard for measuring relative PL quantum yields (QYs).[75] Replicates of three or more were used to measure the absorption and PL emission spectra, and the average QYs recorded.

**Solid-state NMR.** SSNMR spectroscopy experiments (except $^{69}$Ga) were performed on a Bruker wide-bore 9.4 T [$\nu_0(^1H)$ = 400 MHz] NMR spectrometer equipped with a Bruker Advance III HD console. $^7$Li SSNMR spectra were acquired with a Bruker 4 mm HX MAS probe configured in $^1$H–$^7$Li mode. A rotor-synchronized spin-echo pulse sequence was used with 62.5 kHz radio frequency (RF), CT-selective pulses. 3072 scans ($LiGaSe_2$) or 300 scans ($LiInSe_2$) were acquired with a 2 s recycle delay in between scans. The MAS frequency was 10 kHz. $^{77}$Se SSNMR spectra were acquired with a Bruker 2.5 mm HX MAS probe configured in $^1$H–$^{77}$Se mode. A rotor-synchronized spin-echo pulse sequence was used with 83.3 kHz radio frequency (RF), CT-selective pulses. 560 scans were acquired with a 100 s recycle delay in between scans and 23 CPMG loops. The MAS frequency was 22 kHz. $^{69}$Ga SSNMR experiments were performed on a Bruker wide-bore 14.1 T [$\nu_0(^1H)$ = 600 MHz] NMR spectrometer equipped with a Bruker Advance NEO console, WCPMG pulse sequence with a 1 s delay, 25 ms WURST pulse, 12 CPMG loops, 40960 with a Bruker 4 mm HX MAS probe configured in $^1$H–$^{115}$In mode. Peak fitting of the SSNMR spectra was performed in the solid line-shape analysis module version 3.6.3 included in the Bruker Topspin version 3.6.5 software. $^1$H chemical shifts were referenced to tetramethylsilane by using adamantane [$\delta_{iso}(^1H)$ = 1.82 ppm] as a secondary chemical shift standard. $^7$Li, $^{69}$Ga,$^{77}$Se chemical shifts were referenced indirectly to the established chemical shift scale [LiCl, $\delta_{iso}(^7Li)$ = 0 ppm], [$Ga(NO_3)_2$, $\delta_{iso}(^{69}Ga)$ = 0 ppm], [$SeMe_2$, $\delta_{iso}(^{77}Se)$ = 0 ppm] using the previously published relative NMR frequencies.[76]

**Electronic structure calculations.** These were carried out using the Vienna Ab-initio Simulation Package (VASP)[65] and the Tight

Binding Linear Muffin-tin Orbital Atomic Sphere Approximation (TB-LMTO-ASA) package.[66] PBE Band structures and DOS were calculated using the tetrahedron method after converging the total energy on a k-mesh of 1/a×1/b×1/c in the irreducible wedge of the Brillouin zone. Unit cell representations were generated using VESTA.[77]

## Author contributions

Md Riad Sarkar Pavel: writing – original draft, conceptualization, methodology, synthesis and computational investigation. Anuluxan Santhiran: solid state nmr investigation, methodology. Seth Dalberg: synthesis investigation, methodology. Aaron J. Rossini: solid state NMR and writing – review & editing. Javier Vela: supervision, writing – review & editing.

## Conflicts of interest

There are no conflicts to declare.

## Data availability

View Article Online
DOI: 10.1039/D5TA07992F

Data for this article, including powder XRD, electron microscopy images, SS NMR measurements, and DFT calculations are included as part of the Supplementary Information.

## Acknowledgements

This invited manuscript is dedicated to celebrating Prof. D.D. Sarma's contributions to materials science. This work was supported by the U.S. National Science Foundation, Division of Chemistry, Macromolecular, Supramolecular, and Nanochemistry Program (2305062) by a grant awarded to J. V. SSNMR work by A.S. and A.J.R. was supported by the U.S. Department of Energy (DOE) Ames National Laboratory, Materials Science and Engineering Division. Ames National Laboratory is operated for the U.S. DOE by Iowa State University, under contract no. DE-AC02-07CH11358. We thank Gordie Miller and Federico Zahariev for discussions.

## References

[1] J. L. Dye, *Philos. Trans. R. Soc. A,* 2015, **373,** 20140174.
[2] Y. Shen, Z. Zhu, Z. Xu and Y. Li, *Energy Adv.,* 2024, **3,** 1844–1868.
[3] H. Hao, T. Hutter, B. L. Boyce, J. Watt, P. Liu and D. Mitlin, *Chem. Rev.,* 2022, **122,** 8053–8125.
[4] P. Xu, F. Huang, Y. Sun, Y. Lei, X. Cao, S. Liang and G. Fang, *Adv. Funct. Mater.,* 2024, **34,** 2406080.
[5] A. Kausar, A. Sattar, C. Xu, S. Zhang, Z. Kang and Y. Zhang, *Chem. Soc. Rev.,* 2021, **50,** 2696–2736.
[6] A. Van der Ven, Z. Deng, S. Banerjee and S. P. Ong, *Chem. Rev.,* 2020, **120,** 6977–7019.
[7] Y. Zhang, R. Cao, C. Ouyang, L. Jiang, Y. Wang, M. Yang and H. Xia, *J. Mater. Chem. A*, 2025, **13**, 3973–3990.
[8] F. Wu, J. Maier and Y. Yu, *Chem. Soc. Rev.*, 2020, **49**, 1569–1614.
[9] F. Zhang, B. He, Y. Xin, T. Zhu, Y. Zhang, S. Wang, W. Li, Y. Yang and H. Tian, *Chem. Rev.*, 2024, **124**, 4778–4821.
[10] T. Hosaka, K. Kubota, A. S. Hameed and S. Komaba, *Chem. Rev.*, 2020, **120**, 6358–6466.
[11] Y. Zhang, B. Han, S. Tan, Q. Gao, Z. Cai, C. Zhou, J. Li, R. Sun and K. Amine, *Adv. Energy Mater.,* 2025, **15,** 2404796.
[12] H. McKeever, N. N. Patil, M. Palabathuni and S. Singh, *Chem. Mater.,* 2023, **35,** 9833–9846.
[13] C. A. Aranda, A. O. Alvarez, V. S. Chivrony, C. Das, M. Rai and M. Saliba, *Joule,* 2024, **8,** 241–254.
[14] A. Karami, M. Morawski, H. Kempa, R. Scheer and O. Cojocaru-Mirédin, *Sol. RRL,* 2024, **8,** 2300544.
[15] B. A. Tappan and R. L. Brutchey, *ChemNanoMat,* 2020, **6,** 1567–1588.
[16] M. A. White, A. M. Medina-Gonzalez and J. Vela, *Chem. - Eur. J.,* 2018, **24,** 3650–3658.
[17] H. Dong, J. Zhao, H. Yang and Y. Zheng, *Phys. Rev. Mater.,* 2022, **6,** 104001.
[18] L. I. Isaenko and A. P. Yelisseyev, *Semicond. Sci. Technol.,* 2016, **31,** 12300.
[19] N. Jia, S. Wang, P. Wang, C. Li, T. Yu, J. Qiao, C. Li, X. Xiong, J.-L. Sun and X. Tao, *J. Mater. Chem. C,* 2018, **6,** 12615−12622.
[20] T. V. Vu, A. A. Lavrentyev, B. V. Gabrelian, D. D. Vo, P. D. Khang, L. I. Isaenko, S. I. Lobanov, A. F Kurus, and O. Y. Khyzhun, *RSC Adv.,* 2020, **10,** 26843−26852.
[21] Y. Fan, X. Song, S. Qi, X. Ma and M. Zhao, *J. Mater. Chem. A,* 2019, **7,** 26123−26130.
[22] T. Biswas, and A. K. Singh, *Npj Comput. Mater.,* 2021, **7,** 189.
[23] Z. Zheng, H. Yu, M. Zhu, Z. Zhang, Z. Gao, M. Xu, R. Zhang and Y. Xu, *Sci. Rep.,* 2024, **14,** 24779.
[24] Z. Liu, Y. Sun, D. J. Singh and L. Zhang, *Adv. Electron. Mater.,* 2019, **5,** 1900089.
[25] Y. Zhao, L. Huang, D. Zhao and J. Yang Lee, *Angew. Chem. Int. Ed,* 2023, **62,** 202308976.
[26] W. Hua, H. Li, C. Pei, J. Xia, Y. Sun, C. Zhang, W. Lv, Y. Tao, Y. Jiao, B. Zhang and S. Z. Qiao, *Adv. Mater.* 2021, **33,** 2101006.
[27] J. Yang, X. Huang, X. Xu, H. Lu, S. Wang and S. Wu, *ACS Appl. Mater. Interfaces*, 2024, **16**, 15050–15058.
[28] V. Bikbaeva, O. Perez, N. Nesterenko and V. Valtchev, *Inorg. Chem. Front.*, 2022, **9**, 5181–5187.

View Article Online
DOI: 10.1039/D5TA07992F





[29] J. De Roo, *Chem. Mater.*, 2022, **34**, 5766–5779.
[30] M. A. White, K. J. Baumler, Y. Chen, A. Venkatesh, A. M. Medina-Gonzalez, A. J. Rossini, J. V. Zaikina, E. M. Chan and J. Vela, *Chem. Mater.,* 2018, **30,** 6173–6182.
[31] Y. Guo, S. R. Alvarado, J. D. Barclay and J. Vela, *ACS Nano,* 2013, **7,** 3616–3626.
[32] M. P. Hendricks, M. P. Campos, G. T. Cleveland, I. Jen-La Plante and J. S. Owen, *Science,* 2015, **348,** 1226–1230.
[33] M. R. S. Pavel, A. Santhiran, S. Dalberg, A. J. Rossini and J. Vela, *ACS Nano* 2025, **19,** 33413–33422.
[34] M. R. S. Pavel, Y. Chen, A. Santhiran, E. Gi, K. Ochoa-Romero, G. J. Miller, G. Guirado, A. J. Rossini and J. Vela, *ACS Energy Lett.* 2024, **9,** 5012–5018.
[35] B. A. Tappan, G. Barim, J. C. Kwok and R. L. Brutchey, *Chem. Mater.,* 2018, **30,** 5704–5713.
[36] E. J. Endres, J. R. Bairan Espano, A. Koziel, A. R. Peng, A. A. Shults and J. E. Macdonald, *ACS Nanosci. Au*, 2024, **4**, 158–175.
[37] Y. Fu, X. Duan, M. Xing, N. Zhang, X. Luo, H. Wang and Y. Ma, *Mater. Lett.,* 2014, **124,** 141–143.
[38] A. Adhikary, H. Yaghoobnejad Asl, P. Sandineni, S. Balijapelly, S. Mohapatra, S. Khatua, S. Konar, N. Gerasimchuk, A. V. Chernatynskiy and A. Choudhury, *Chem. Mater.,* 2020, **32,** 5589–5603.
[39] V. V. Klepov, A. A. Berseneva, K. A. Pace, V. Kocevski, M. Sun, P. Qiu, H. Wang, F. Chen, T. M. Besmann and H. C. Zur Loye, *Angew. Chem., Int. Ed.,* 2020, **59,** 10836–10841.
[40] S. F. Li, X. M. Jiang, B. W. Liu, D. Yan, C. S. Lin, H. Y. Zeng and G. C. Guo, *Chem. Mater.,* 2017, **29,** 1796–1804.
[41] Z. Sun, C. M. Perez, O. V. Prezhdo and R. L Brutchey, *ACS Nanoscience Au,* 2024, **4,** 381–390.
[42] Z. Sun, C. P. Pakhanyan, U. Saleem, E. I. Feldman, S. Mallikarjun Sharada and R. L. Brutchey, *Inorg. Chem*. 2025, **64**, in press. DOI: 10.1021/acs.inorgchem.5c04153.
[43] S. K. O'Boyle, A. Naeem and R. E. Schaak, *Chem. Mater*. 2025, **37**, in press. DOI: 10.1021/acs.chemmater.5c02079.
[44] H. Yan, L. Chen, L. Feng, Y. Chen, M. Zhang and Q. Wei, *Vacuum,* 2024, **225,** 113256.
[45] R. F. Ali and B. D. Gates, *Nanoscale*, 2021, **13,** 3214–3226.
[46] C.-Y. Yeh, Z. Lu, S. Froyen and A. Zunger, *Phys. Rev. B: Condens. Matter Mater. Phys.,* 1992, **46,** 10086–10097.
[47] Y. E. Maidebura, V. G. Mansurov, T. V. Malin, I. A. Aleksandrov, K. S. Zhuravlev and B. Pecz, *CrystEngComm*, 2025, **27,** 2307–2316.
[48] N. Kapuria, B. Nan, T. E. Adegoke, U. Bangert, A. Cabot, S. Singh and K. M. Ryan, *Chem. Mater.*, 2023, **35**, 4810–4820.
[49] M. Strach, V. Mantella, J. R. Pankhurst, P. Iyengar, A. Loiudice, S. Das, C. Corminboeuf, W. van Beek and R. Buonsanti, *J. Am. Chem. Soc.*, 2019, **141**, 16312–16322.
[50] R. K Harris, E. D. Becker, S. M. Cabral de Menezes, R. Goodfellow and P. Granger, *Pure Appl. Chem.,* 2001, **73,** 1795–1818.
[51] S. E. Ashbrook, *Phys. Chem. Chem. Phys.,* 2009, **11,** 6892–6905.
[52] S. E. Ashbrook and S. Sneddon, *J. Am. Chem. Soc.,* 2014, **136,** 15440–15456.
[53] R. W. Schurko, *Acc. Chem. Res.,* 2013, **46,** 1985–1995.
[54] L. A. O'Dell, A. J. Rossini and R. W. Schurko, *Chem. Phys. Lett.,* 2009, **468,** 330–335.
[55] W. H. Dawson, J. D. Odom, *J. Am. Chem. Soc.,* 1977, **99,** 8352–8354.
[56] J. D. Odom, W. H. Dawson and P. D. Ellis, *J. Am. Chem. Soc.,* 1979, **101,** 5815–5822.
[57] A. Eifler, V. Riede, J. Brückner, S. Weise, V. Krämer, G. Lippold, W. Schmitz, K. Bente and W. Grill, *Jpn. J. Appl. Phys.,* 2000, **39,** 279-1–279-4.
[58] L. Isaenko, I. Vasilyeva, A. Yelisseyev, S. Lobanov, V. Malakhov, L. Dovlitova, J. J. Zondy and I. Kavun, *J. Cryst. Growth,* 2000, **218,** 313–322.
[59] M. Jomaa, V. Mishra, D. Mumbaraddi, R. Sikdar, D. Sarkar, M. Sun, J. Yao, V. K. Michaelis and A. Mar, *Inorg. Chem.,* 2023, **62,** 7491–7502.
[60] D. Clark, J. Zhang, A. Craig, A. Weiland, J. Brant, J. Cho, Y. Kim, J. Jang and J. Aitken, *J. Alloys Compd.,* 2022, **917,** 165381-1–165381-12.
[61] E. Tupitsyn, P. Bhattacharya, E. Rowe, L. Matei, Y. Cui, V. Buliga, M. Groza, B. Wiggins, A. Burger and A. Stowe, *J. Cryst. Growth,* 2014, **393,** 23–27.
[62] L. Isaenko, A. Yelisseyev, S. Lobanov, V. Petrov, F. Rotermund, G. Slekys and J.-J. Zondy, *J. Appl. Phys.,* 2002, **91,** 9475–9480.
[63] L. Guo, Y. Xu, H. Zheng, W. Xue, J. Dong, B. Zhang, Y. He, G. Zha, D. Y. Chung, W. Jie and M. G. Kanatzidis, *Cryst. Growth Des.,* 2018, **18,** 2864–2870.
[64] A. K. P. Mann, S. Wicker and S. E. Skrabalak, *Adv. Mater.,* 2012, **24,** 6186–6191.
[65] G. Kresse and J. Furthmuller, *Comput. Mater. Sci.,* 1996, **6,** 15–50.
[66] O. Jepsen, A. Burkhardt and O. K. Andersen, The Program TB-LMTO-ASA, version 4.7; Max-Planck-Institut fur Festkorperforschung: Stuttgart, Germany, 1999.
[67] G. J. Miller, *Eur. J. Inorg. Chem.*, 1998, **1998**, 523–536.
[68] B. A. Rosales, M. A. White and J. Vela, J. Am. Chem. Soc., 2018, **140,** 3736-3742.
[69] P. Mori-Sánchez, A. J. Cohen and W. Yang, *Phys. Rev. Lett.,* 2008, **100,** 146401-1–146401-4.
[70] A. A. Lavrentyev, B. V. Gabrelian, V. T. Vu, L. N. Ananchenko, L. I. Isaenko, A. P. Yelisseyev and O. Y. Khyzhun, *Opt. Mater.,* 2017, **66,** 149–159.
[71] W. Chen, J. M. Zhang, Q. L. Xia, Y. Z. Nie and G. H. Guo, *Phys. Chem. Chem. Phys.,* 2020, **22,** 16007–16012.
[72] M. S. Khan, B. Gul, G. Khan, S. A. Khattak, M. Ajaz, T. Khan and S. Zulfiqar, *J. Solid State Chem.,* 2022, **307,** 122853-1–122853-12.
[73] W. B. Cai, A. Abudurusuli, C. W. Xie, E. Tikhonov, J. J. Li, S. L. Pan and Z. H. Yang, *Adv. Funct. Mater.,* 2022, **32,** 2200231-1–2200231-8.

View Article Online
DOI: 10.1039/D5TA07992F



[74] B. D. Viezbicke, S. Patel, B. E. Davis and D. P. Birnie, *Phys. Status Solidi B,* 2015, **252,** 1700–1710.
[75] M. Grabolle, M. Spieles, V. Lesnyak, N. Gaponik, A. Eychmüller and U. Resch-Genger, *Anal. Chem.,* 2009, **81,** 6285–6294.
[76] R. K. Harris, E. D. Becker, S. M. Cabral de Menezes, R. Goodfellow and P. Granger, *Solid State Nucl. Magn. Reson.,* 2002, **22,** 458–483.
[77] K. Momma and F. Izumi, *J. Appl. Crystallogr.,* 2011, **44,** 1272–1276.

View Article Online
DOI: 10.1039/D5TA07992F

## Data Availability

Data for this article, including powder XRD, electron microscopy images, SS NMR measurements, and DFT calculations are included as part of the Supplementary Information.